J. Fluid Mech. (2010), *vol.* 648, *pp.* 53–82.
doi:10.1017/S0022112009993442

Experimental and theoretical study of vibration-induced thermal convection in low gravity

VALENTINA SHEVTSOVA†, ILYA I. RYZHKOV, DENIS E. MELNIKOV, YURI A. GAPONENKO AND ALIAKSANDR MIALDUN

Microgravity Research Centre, Université Libre de Bruxelles, CP-165/62 av. F. D. Roosevelt, 50, B-1050 Brussels, Belgium

(Received 2 August 2009; revised 11 November 2009; accepted 12 November 2009)

Vibrations acting on a fluid with density gradient induced by temperature variations can cause relative flows. High-frequency vibration leads to the appearance of time-averaged (mean) flows (or streaming flows), which can essentially affect heat and mass transfer processes. This phenomenon is most pronounced in the absence of other external forces (in particular, static gravity). In this work, an extensive experimental and computational study of thermal vibrational convection in a reduced-gravity environment of a parabolic flight is performed. The transient evolution of the temperature field in a cubic cell subjected to translational vibration is investigated by optical digital interferometry. The mean flow structures previously reported in numerical studies are confirmed. The transition from four-vortex flow to a pattern with a large diagonal vortex and two small vortices is observed in the transient state. The experiments reveal a significant enhancement of heat transfer by vibrational mean flows with increasing the vibrational strength. Three-dimensional direct numerical simulation with real microgravity profile and two-dimensional numerical modelling based on averaging approach provide a very good agreement with the experimental results. The influence of residual gravity on heat transfer and bifurcation scenario is first investigated numerically and correlated with the experimental data. It is demonstrated that gravity effects on non-uniformly heated fluids can be reproduced in weightlessness by applying vibrations to the system.

1. Introduction

The application of vibrations to a fluid system with density gradient can cause relative flows inside the fluid. If this gradient results from thermal or compositional variations, such flows are known as thermovibrational or solutovibrational convection, respectively. The response of the fluid to external forcing depends on the frequency of vibration. One can speak about low or high frequencies depending on whether the period is comparable to or much smaller than the reference viscous and heat/mass diffusion times. The high-frequency limit is of special interest: here the flow can be represented as a superposition of the 'fast' part, which oscillates with the frequency of imposed vibration, and the 'slow' time-averaged part (mean flow), which describes the

† Email address for correspondence: vshev@ulb.ac.be

nonlinear response of the fluid to a periodic excitation (Gershuni & Lyubimov 1998). In the theory of convection, the averaging approach was first used by Zenkovskaya & Simonenko (1966). Mean flows, also referred to as streaming flows, can contribute to the transport of heat and mass in the time-averaged sense. This contribution is most pronounced in the absence of other external forces (in particular, static gravity).

The study of vibrational impact on fluids has fundamental and applied importance. Vibrational convection is an additional way of transporting heat and matter in weightlessness similar to thermocapillary and solutocapillary convection. Mean flows show some similarity with flows induced by the static gravity and might serve as a way to control and operate fluids in space (Beysens 2006). Vibrations can suppress or intensify gravitational convection depending on the mutual orientation of vibration axis and thermal or compositional gradient (Savino & Monti 1998). High-frequency oscillations (g-jitter) on-board microgravity platforms can disturb the experiments that require purely diffusive heat and mass transfer, such as crystal growth and measurement of transport coefficients. This problem was addressed in the comprehensive works of Alexander (1990) and Savino & Monti (2001). The results of Shevtsova, Melnikov & Legros (2004) are complementary to them.

There have been extensive theoretical studies of thermovibrational convection in various configurations and under different gravity levels. Using the averaging method, Gershuni, Zhukhovitskii & Yurkov (1982) performed one of the first numerical simulations of vibrational convection in rectangular and square cavities in weightlessness. Biringen & Danabasoglu (1990) investigated gravity modulation effect on thermal convection in microgravity and terrestrial conditions by solving the full-nonlinear Boussinesq equations. Savino, Monti & Piccirillo (1998) studied vibrational mean flows in a cubic cavity and found qualitative similarity between three-dimensional results and previous two-dimensional simulations. The impact of intensity and direction of vibration on convective instability in rectangular cavities with different aspect ratios was analysed by Cisse, Bardan & Mojtabi (2004). Demin, Gershuni & Verkholantsev (1996) showed that in an infinite plane layer, the onset of instability essentially depends on the angle between the temperature gradient and the direction of vibration. Farooq & Homsy (1994, 1996) studied the interaction of small harmonic oscillations with the flow produced by the static gravity field. The possibility of resonances between the basic flow and higher-order streaming induced by vibrations was shown. A parametric study of convection in a square cavity over a wide range of frequencies and amplitudes was performed by Hirata, Sasaki & Tanigawa (2001). In different parametric ranges, they observed synchronous, sub-harmonic and non-periodic responses of the system to external forcing. The influence of vibrations on the stability of a horizontal, binary-mixture layer with the Soret effect was investigated by Gershuni *et al.* (1997). Shevtsova *et al.* (2007) studied the impact of vibration on thermal diffusion separation of binary mixture in a cubic cavity.

Ground-based experiments on vibrational convection have been performed in a number of works. Zavarykin, Zorin & Putin (1988) investigated the stability of quasi-equilibrium in a horizontal fluid layer heated from above and below under transversal vibration. These results are in good agreement with theoretical predictions summarized by Gershuni & Lyubimov (1998). Spatiotemporal behaviour of instabilities in a Rayleigh–Bénard cell under gravity modulation was analysed by Ishikawa & Kamei (1993). Ivanova & Kozlov (2003) investigated the combined action of translational and rotational vibrations on the fluid in a plane layer. Recently, Babushkin &

Demin (2006) studied thermovibrational flows in a Hele–Shaw cell. The observed flow structures were confirmed by numerical modelling.

The experimental studies of vibrational phenomena in weightlessness are rather limited. A series of experiments was carried out with the ALICE-2 instrument on-board the MIR station by Zyuzgin *et al.* (2001) and Garrabos *et al.* (2007). The influence of vibrations on the propagation of a temperature wave from a heat source in a near-critical fluid was investigated. The thermovibrational flows were registered by observing the optical inhomogeneity caused by the distortion of the temperature field. It was not possible to reconstruct this field quantitatively. The impact of residual accelerations on-board a spacecraft on convection in differentially heated cylindrical cavities was studied independently by Babushkin *et al.* (2001) and Naumann *et al.* (2002). In these experiments, the temperature field was monitored at several fixed points. The results did not provide clear evidence of time-averaged flows and the related heat transfer caused by periodic high-frequency g-jitter.

In the current work, we present an extensive experimental and numerical study of thermovibrational convection in a low-gravity environment of a parabolic flight ($g \sim 10^{-2} g_0$, where g_0 is the gravity level on Earth). The fluid is confined in a cubic cell with differentially heated walls and is subjected to translational vibration perpendicular to the temperature gradient. Despite a large number of theoretical works mentioned above, this configuration has never been studied experimentally in either weightlessness or ground conditions. The main goals of the experiment are as follows: (*a*) to observe and interpret vibrational mean flows and related heat transfer in low gravity and (*b*) to verify the existing theoretical studies. Because of the relatively short microgravity time available in parabolic flights, the experimental study is focused on transient development of thermovibrational convection. Complementary theoretical and numerical analysis is aimed at extending the previous results and assessing unique experimental conditions of our study. The preparation of this experiment was reported earlier by Melnikov *et al.* (2008), while the first experimental results were concisely presented by Mialdun *et al.* (2008*a*,*b*).

The paper is organized as follows. In § 2, we describe the experimental set-up and microgravity environment of a parabolic flight. Mathematical models used for numerical simulation are presented in § 3. We employ three-dimensional Navier–Stokes and heat transfer equations as well as two-dimensional equations based on the averaging approach. Preliminary theoretical and numerical analysis of the impact of residual gravity on the flow structure and transient behaviour of the system is performed in § 4. The experimental results and comparison with numerical simulations are presented in § 5.

2. The experiment

2.1. *Experimental set-up*

To observe thermovibrational convection in microgravity, we have designed a special experimental set-up (figure 1). The working liquid is placed in a cubic cell with transparent walls of internal size $L = 5$ mm. The external walls of the cell are shaped in the form of two prisms (figure 1*c*) to allow optical observation (see the description below). The cell is made of quartz Suprasil. The top and bottom walls are kept at constant temperatures T_{hot} and T_{cold}, respectively, by Peltier modules (3×3 cm). In the experiments, the mean temperature $(T_{cold}+T_{hot})/2$ was fixed at 40°C, while the applied temperature difference $\Delta T = T_{hot}-T_{cold}$ was either 15 K or 20 K. The experimental cell is attached to the linear motor, which performs translational harmonic oscillations in

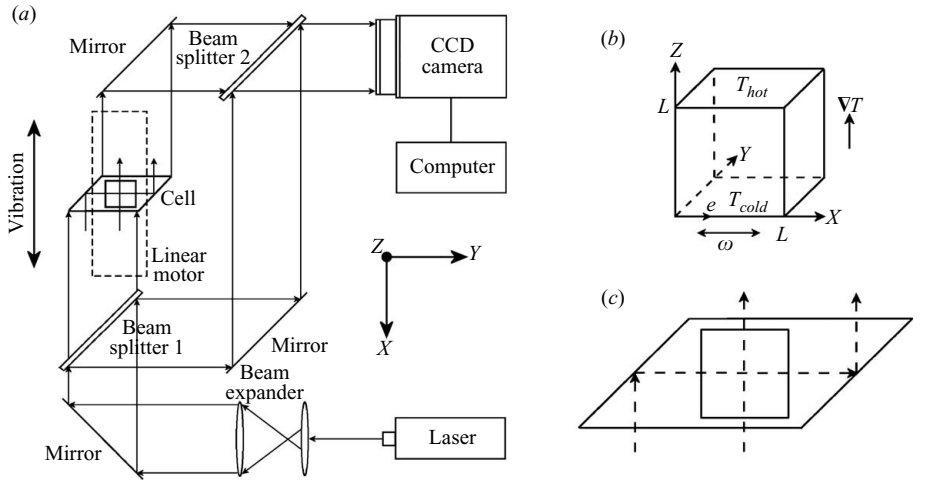

FIGURE 1. (*a*) The scheme of experimental set-up, (*b*) the cubic cell and coordinate system and (*c*) the top view of the experimental cell.

L (m)	ρ_0 (kg m^{-3})	β_T (10^{-3} K^{-1})	ν (10^{-6} m^2 s^{-1})	χ (10^{-7} m^2 s^{-1})	τ_{vs} (s)	τ_{th} (s)	Pr
0.005	769	1.095	1.730	0.623	14.5	401.3	27.8

TABLE 1. The main parameters of the system: the cell size, physical properties of isopropanol at 40°C, characteristic viscous time $\tau_{vs} = L^2/\nu$ and thermal time $\tau_{th} = L^2/\chi$ and the Prandtl number $Pr = \nu/\chi$.

the X-direction (perpendicular to the temperature gradient). The mass of the moving part was 2.5 kg. In the experiments, the frequency and amplitude were varied in the ranges 1–12 Hz and 10–140 mm, respectively. The maximum vibrational acceleration $A\omega^2 = 5.8\, g_0$ was achieved at $A = 10$ mm and $f = 12$ Hz ($\omega = 2\pi f$). The upper limit for frequency increases with decreasing the amplitude.

The working liquid was isopropanol at the mean temperature of 40°C. The liquid is characterized by the density ρ_0, thermal expansion β_T, kinematic viscosity ν and thermal diffusivity χ. These properties are listed in table 1 along with the other parameters of the system, which are relevant to our study.

The thermovibrational flows were monitored by measuring the temperature field inside the cell by optical digital interferometry. The set-up is based on the concept of Mach–Zehnder interferometer (figure 1). The light beam of He-Ne laser (wavelength of 632.8 nm) is enlarged and collimated by the beam expander and then splitted into two parallel beams of equal intensity by the beam splitter. One of the beams traverses the entire cell in two perpendicular directions. The lateral walls shaped in the form of two transparent prisms allow scanning the front and side views (planes YZ and XZ, respectively). The beam paths through the cell are shown by the arrows. The temperature variations in the liquid create the spatial distribution of refractive index that modulates the wavefront of the emerging optical beam. After passing the mirror, this beam interferes with the reference one at the second beam splitter. An example of interference pattern with front and side views of the cell is shown in figure 2. The patterns are recorded by a CCD camera (24 fps, 1280×1024 pixels

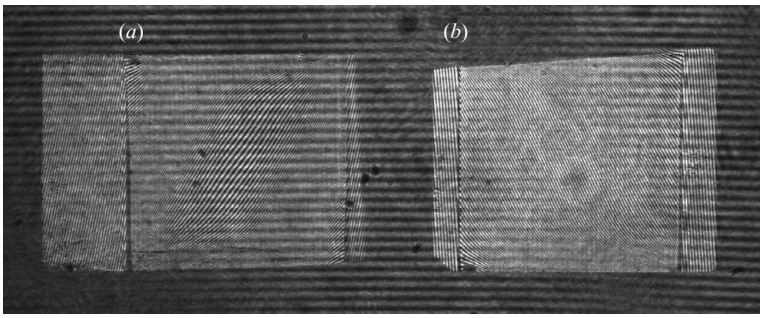

FIGURE 2. Interference pattern of the cell: (*a*) side view and (*b*) front view.

sensor) and processed by a computer. Interferograms are reconstructed by performing two-dimensional fast Fourier transform (FFT) of the fringe image, filtering a selected band of spectrum, performing the inverse two-dimensional FFT of the filtered result and phase unwrapping. The knowledge of phase shift gives information about the gradient of refractive index, which is used to reconstruct two-dimensional projections of the temperature field on the front and side view planes. This method allows temperature measurement with the accuracy of 0.01 K. More details about optical digital interferometry can be found in Mialdun & Shevtsova (2008).

The velocity field in the cell is observed with a help of tracer particles (hollow ceramic microspheres with the radius 75 ± 20 μm). The availability of two perpendicular views of the cell allows us to determine three-dimensional coordinates (positions) of the tracer particles from fringe images (see figures 2 and 10). The experimental trajectories of particles are restored by processing successive images, which are recorded during an experimental run.

2.2. *Microgravity environment*

The experiments were performed in parabolic flights during the 46th and 48th campaigns organized by the European Space Agency in November 2007 and March 2008, respectively. Parabolic flights provide repeated periods of 20–22 s of reduced gravity (or 'microgravity') with $g \sim 10^{-2} g_0$, where $g_0 = -9.81\,\mathrm{m\,s^{-2}}$ is the gravity level on Earth. These periods are preceded and followed by 20 s of hypergravity reaching up to $1.8 g_0$. During one flight, a total of 31 parabolas is performed; each campaign includes three flights. Figure 3(*a*) shows a typical gravity profile during a single parabola. The microgravity period is delimited by the dashed lines and is shown on a larger scale in figure 3(*b*). The residual-gravity level is

$$|g_x|,\ |g_y| \leqslant 10^{-2} g_0, \qquad |g_z| \leqslant 5 \times 10^{-2} g_0. \tag{2.1}$$

Here the X and Y axes lie in the plane of aircraft wings (the positive X-axis points towards the nose). The Z-axis is perpendicular to the plane of the wings and goes out of the upper side of the vehicle. The experimental set-up was placed in a specially designed rack and installed in the aircraft. The orientation of the experimental cell with respect to the described coordinate system is shown in figure 1(*b*). The gravity level during the flight was measured by an accelerometer with the sampling rate of 5 Hz. The accelerometer was mounted on the experimental set-up.

The scenario of the experiment is as follows. The temperature gradient is established in the cell during horizontal flight. To suppress convection, the cell is heated from above (the temperature gradient is co-directed with the Z-axis of the aircraft and is opposed to the gravity vector). Vibration is switched on in the beginning of

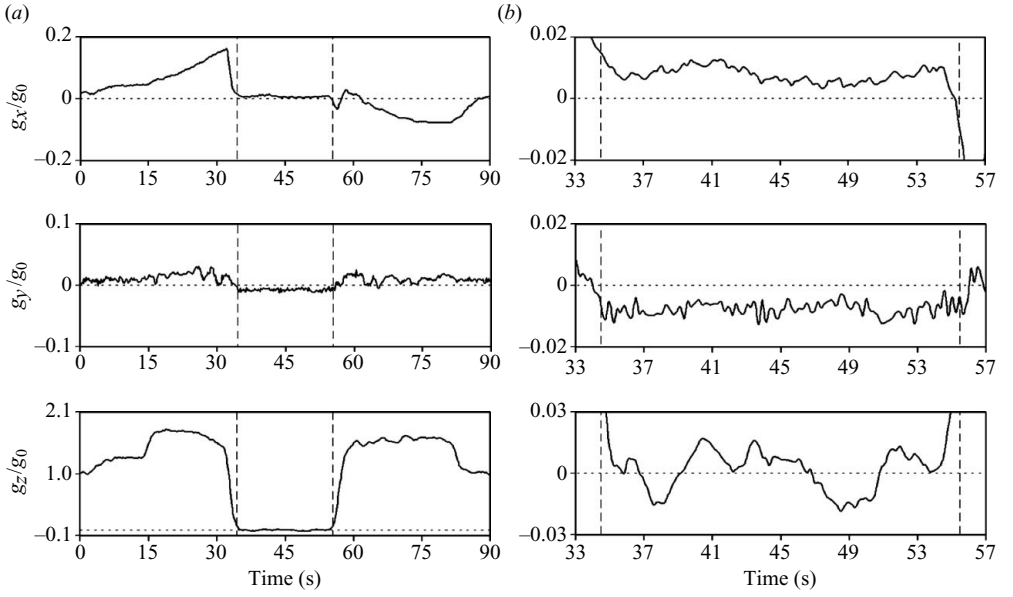

FIGURE 3. Acceleration profiles (a) during a parabolic flight manoeuvre and (b) during microgravity period.

microgravity and continues for 25 s (slightly larger than microgravity time). During this time, interferometric patterns are recorded by the camera. The motor is switched off after the end of the microgravity period. The time of horizontal flight between two consecutive parabolas is around 2 min. A large number of available parabolas allowed us to perform repeated experiments with the same configuration as well as to investigate different vibrational regimes.

3. Mathematical formulation

3.1. *Full-nonlinear equations*

In this section, we describe mathematical models which are used for numerical simulation of gravitational and thermovibrational convection in a cubic cell. The geometry of the cell is presented in figure 1(b). In the coordinate system associated with the cell, the acceleration applied to the system is the sum of gravitational and vibrational accelerations:

$$\boldsymbol{g}(t) + A\omega^2 \cos(\omega t)\, \boldsymbol{e},$$

where $\boldsymbol{g}(t) = (g_x, g_y, g_z)$ is the time-dependent gravity vector and $\boldsymbol{e} = (1, 0, 0)$ is the unit vector along the axis of vibrations. The problem is considered in Boussinesq approximation, and the density is written as

$$\rho = \rho_0\big(1 - \beta_T T\big),$$

where T is the deviation of temperature from T_{cold}. The equations of motion and heat transport are written as

$$\left.\begin{aligned} &\partial_t \boldsymbol{V} + (\boldsymbol{V}\cdot\nabla)\,\boldsymbol{V} = -\rho_0^{-1}\nabla P + \nu\nabla^2\boldsymbol{V} + (1-\beta_T T)\big(\mathbf{g}(t) + A\omega^2\cos(\omega t)\,\boldsymbol{e}\big),\\ &\partial_t T + \boldsymbol{V}\cdot\nabla\, T = \chi\nabla^2 T,\\ &\nabla\cdot\boldsymbol{V} = 0. \end{aligned}\right\} \quad (3.1)$$

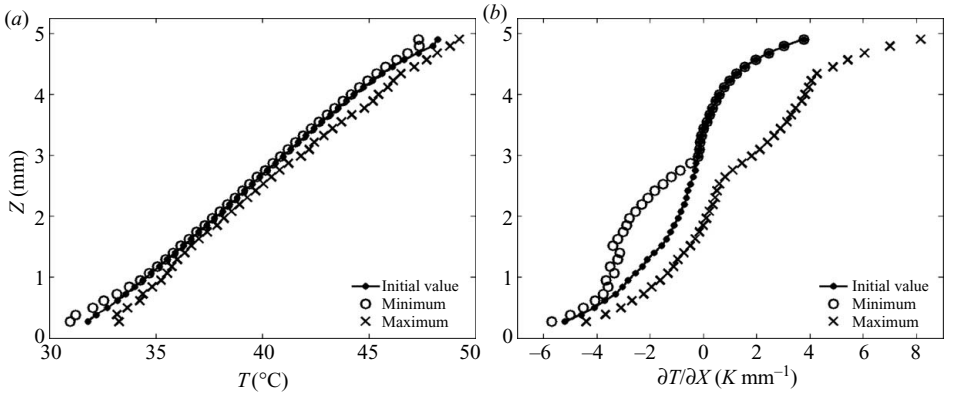

FIGURE 4. (*a*) The temperature profile and (*b*) the temperature gradient on the lateral wall $X = 0$. The initial, minimum and maximum values over the experimental run (22 s) are shown.

The validity of Boussinesq approximation for the present system is justified in the Appendix.

Let us introduce dimensionless variables by taking the scales of length L, time L^2/ν, velocity ν/L, pressure $\rho_o \nu^2/L^2$ and temperature $\Delta T = T_{hot} - T_{cold}$. The dimensionless equations are written in the form

$$\left.\begin{aligned} &\partial_t \boldsymbol{v} + (\boldsymbol{v}\cdot\nabla)\,\boldsymbol{v} = -\nabla p + \nabla^2 \boldsymbol{v} - Pr^{-1}\big(\boldsymbol{Ra}(t) + Ra_{os}\cos(\Omega t)\,\boldsymbol{e}\big)\,\Theta,\\ &\partial_t \Theta + \boldsymbol{v}\cdot\nabla\Theta = Pr^{-1}\,\nabla^2\Theta,\\ &\nabla\cdot\boldsymbol{v} = 0, \end{aligned}\right\} \tag{3.2}$$

In these equations, $p = \widetilde{P}L^2/\rho_0\nu^2$, where the modified pressure is defined by

$$\widetilde{P} = P - \rho_0\big(\mathbf{g}(t) + A\omega^2\cos(\omega t)\,\boldsymbol{e}\big)\cdot\boldsymbol{X} \tag{3.3}$$

with $\boldsymbol{X} = (X, Y, Z)$. The system includes the Prandtl number Pr, the Rayleigh numbers $\boldsymbol{Ra}(t) = (Ra_x,\ Ra_y,\ Ra_z)$, the oscillatory Rayleigh number Ra_{os} and the dimensionless angular frequency Ω:

$$Pr = \frac{\nu}{\chi}, \quad Ra_{x,y,z} = \frac{g_{x,y,z}\beta_T \Delta T L^3}{\nu\chi}, \quad Ra_{os} = \frac{A\omega^2\beta_T\Delta T L^3}{\nu\chi}, \quad \Omega = \frac{\omega L^2}{\nu}. \tag{3.4}$$

The oscillatory Rayleigh number can be regarded as a ratio of the vibrational buoyancy force to the product of momentum and thermal diffusivities.

The cell boundaries are rigid with the no-slip condition for the velocity. The bottom and top walls are kept at constant temperatures T_{cold} and T_{hot}, respectively. So, the dimensionless boundary conditions of the problem are given by

$$x, y, z = 0, 1: \quad \boldsymbol{v} = 0; \qquad z = 0: \quad \Theta = 0; \qquad z = 1: \quad \Theta = 1 \tag{3.5}$$

To impose conditions on the lateral walls, we refer to the experimental measurements. Figure 4(*a*) shows the temperature profile at the lateral wall $X = 0$, while the temperature gradient, which is proportional to the heat flux through the wall, is presented in figure 4(*b*). Measurements reveal that the flux is non-zero; in addition, it is changing with time. However, the temperature distribution on the walls is very close to linear, and its variation with time is small. So, we impose a linear temperature profile on the lateral boundaries:

$$x, y = 0, 1: \quad \Theta = z. \tag{3.6}$$

The temperature gradient is established before the start of the experiment; so the initial conditions are given by

$$t = 0: \quad \boldsymbol{v} = 0, \qquad \Theta = z. \tag{3.7}$$

To investigate the transfer of heat by vibrational flow, we introduce the dimensionless heat flux through the walls (the Nusselt number), which is defined by

$$Nu(t) = \frac{1}{2} \oint_{\Gamma} \left| \frac{\partial T}{\partial n} \right| \mathrm{d}S. \tag{3.8}$$

Here $\partial T/\partial n$ is the normal component of the temperature gradient ($\boldsymbol{n}$ is the outward unit normal to the boundary of the cavity Γ). In the case of purely diffusive heat transfer, one has $Nu = 1$. The difference $Nu - 1$ measures convective contribution to the transport of heat. It should be noted that the Nusselt number (3.8) describes the amount of heat (in dimensionless units) which is transferred through the liquid volume. To show this, let us introduce two Nusselt numbers

$$Nu^{+} = \oint_{\Gamma} \frac{\partial T}{\partial n} \mathrm{d}S \left(\frac{\partial T}{\partial n} > 0 \right), \qquad Nu^{-} = \oint_{\Gamma} \frac{\partial T}{\partial n} \mathrm{d}S \left(\frac{\partial T}{\partial n} < 0 \right),$$

which describe the heat gain (heat loss) by the fluid through the walls, respectively. Assuming that there is no internal heat sources and the amount of heat resulting from viscous dissipation is negligible, we have $Nu^{+} + Nu^{-} = 0$. Then it is clear that $Nu = (1/2)(Nu^{+} - Nu^{-}) = Nu^{+} = -Nu^{-}$.

3.1.1. *Numerical method*

The three-dimensional problem (3.2)–(3.6) is discretized by using the finite-volume technique on a staggered grid where the pressure and temperature nodes are placed at the centre of control volumes and the velocity components are positioned at the faces of these volumes. The discretized equations are solved by an explicit single forward time step marching method. Computation of the velocity field at each time step is carried out by the projection method (Chorin 1968). The main idea of the method is that the initial momentum equation can be splitted into two independent ones. At first, a 'provisional' velocity field corresponding to the correct vorticity but not satisfying the continuity equation is computed neglecting the pressure gradient in the momentum equation. The equation defining the velocity field on the next time level includes only the pressure gradient term. To calculate the pressure, the Poisson equation is solved. It is discretized using the combination of FFT (DFFT) in the y-direction and an implicit alternating direction implicit (ADI) method at the other directions. The discretized Laplace equation for the pressure is solved by the iterative algorithm. After calculating the 'provisional' velocity and pressure, we advance in time and obtain the values of velocity and temperature.

In order to confirm the accuracy of numerical method, we have conducted simulations for different sizes of an equally spaced mesh. The results are presented in table 2 for the following values of parameters: $\Delta T = 20$ K, $f = 4$ Hz, $A = 45$ mm, $\boldsymbol{g} = 0$. The control parameters are the Nusselt number on the hot wall (averaged over the period) and variation of maximum dimensionless velocity during the period of oscillation. The presented values correspond to one thermal time $\tau_{th} = 401.3$ s from the start of vibration. The regular mesh $[32 \times 33 \times 32]$ is finally chosen for the calculations, as further refinement has little effect on the values of control parameters. Using this mesh, we have investigated the time step sensitivity of the numerical scheme

Mesh size $[n_x \times n_y \times n_z]$	Nu^{hot}	$\max \lvert \boldsymbol{v} \rvert$
$12 \times 9 \times 12$	1.654	4.726–16.467
$32 \times 33 \times 32$	1.554	6.386–17.709
$42 \times 33 \times 42$	1.546	6.302–17.658

TABLE 2. The Nusselt number on the hot wall (averaged over the period) and variation of maximum velocity during the period of oscillation.

by varying the dimensionless time step between 10^{-5} and 10^{-4}. Negligible variations of the Nusselt number (within 0.1 %) and maximum velocity (within 0.01 %) with changing the time step were found. It guarantees the temporal convergence of the employed numerical method. In the calculations below, the dimensionless time step is taken as 10^{-4}. Note that this choice provides 57 time steps per period for the maximum frequency used in the calculations (12 Hz).

3.2. *Averaging approach*

In the limit of vibrations with high frequency and small amplitude, the method of averaging can be effectively applied for studying thermovibrational convection (see Zenkovskaya & Simonenko 1966; Gershuni & Lyubimov 1998).

Let us denote the period of vibration by $\tau = 2\pi/\omega$. In the averaging method, each field is decomposed into the 'slow' time-averaged part (with characteristic time much larger than τ) and the 'fast' oscillatory part (with characteristic time τ):

$$\boldsymbol{V} = \overline{\boldsymbol{V}} + \boldsymbol{V}', \qquad T = \overline{T} + T', \qquad \widetilde{P} = \overline{P} + P' \tag{3.9}$$

(see (3.3)). The time-averaged (mean) velocity and temperature fields are defined by

$$\overline{\boldsymbol{V}}(t) = \frac{1}{\tau}\int_{t-\tau/2}^{t+\tau/2} \boldsymbol{V}(\tau')\,\mathrm{d}\tau', \qquad \overline{T}(t) = \frac{1}{\tau}\int_{t-\tau/2}^{t+\tau/2} T(\tau')\,\mathrm{d}\tau'. \tag{3.10}$$

Mean pressure is defined similarly. The derivation of equations for averaged fields can be found in Gershuni & Lyubimov (1998). The averaging approach is valid under the following assumptions:

(i) The period of vibration is much smaller than the reference viscous and thermal times,

$$\tau \ll \min(L^2/\nu,\ L^2/\chi). \tag{3.11}$$

In addition, it satisfies

$$\tau \ll \sqrt{\frac{L}{g\beta_T \Delta T}}. \tag{3.12}$$

This inequality is derived from the requirement that the gravitational buoyancy force induced by the oscillatory temperature component is much smaller than the vibrational buoyancy force induced by the same component.

(ii) The amplitude of vibration satisfies the inequality

$$A \ll \frac{L}{\beta_T \Delta T}. \tag{3.13}$$

This assumption follows from the requirement that the displacement of fluid particles during one period of oscillation is much smaller than the characteristic length scale.

The averaged equations of thermovibrational convection have the form

$$\left.\begin{aligned}
&\partial_t \overline{\boldsymbol{V}} + (\overline{\boldsymbol{V}}\cdot\nabla)\overline{\boldsymbol{V}} = -\rho_0^{-1}\nabla\overline{P} + \nu\nabla^2\overline{\boldsymbol{V}} - \beta_T\overline{T}\boldsymbol{g} + \frac{(\beta_T A\omega)^2}{2}\big((\overline{T}\boldsymbol{e} - \nabla\Phi)\cdot\nabla\big)\nabla\Phi,\\
&\partial_t\overline{T} + (\overline{\boldsymbol{V}}\cdot\nabla)\overline{T} = \chi\nabla^2\overline{T},\\
&\nabla\cdot\overline{\boldsymbol{V}} = 0,\\
&\nabla^2\Phi - \nabla\overline{T}\cdot\boldsymbol{e} = 0.
\end{aligned}\right\} \tag{3.14}$$

Here a new function Φ results from the decomposition of the vector $\overline{T}\boldsymbol{e}$ into its solenoidal and irrotational parts, $\boldsymbol{W}$ and $\nabla\Phi$ respectively:

$$\overline{T}\boldsymbol{e} = \boldsymbol{W} + \nabla\Phi, \qquad \nabla\cdot\boldsymbol{W} = 0. \tag{3.15}$$

The oscillatory fields satisfy the equations

$$\left.\begin{aligned}
&\partial_t\boldsymbol{V}' = -\rho_0^{-1}\nabla P' - \beta_T\overline{T}A\omega^2\cos(\omega t)\boldsymbol{e},\\
&\partial_t T' = -\boldsymbol{V}'\cdot\nabla\overline{T},\\
&\nabla\cdot\boldsymbol{V}' = 0.
\end{aligned}\right\} \tag{3.16}$$

The solution of this system can be obtained with the help of (3.15):

$$\left.\begin{aligned}
&\boldsymbol{V}' = -\beta_T A\omega\sin(\omega t)\boldsymbol{W}, \qquad T' = -\beta_T A\cos(\omega t)\boldsymbol{W}\cdot\nabla\overline{T},\\
&P' = -\rho_0\beta_T A\omega^2\cos(\omega t)\,\Phi
\end{aligned}\right\} \tag{3.17}$$

(see Gershuni & Lyubimov 1998 for the details). It should be noted that under assumption (3.11), the viscous force term driving the oscillatory flow was neglected in the derivation. Thus, the existence of the Stokes boundary layer for the oscillatory flow is not taken into account. So, the non-permeability condition rather than the no-slip one should be imposed on the oscillatory velocity component $\boldsymbol{V}'$ and, correspondingly, on the function $\boldsymbol{W}$:

$$\boldsymbol{W}\cdot\boldsymbol{n}\big|_{\Gamma} = 0. \tag{3.18}$$

Here $\boldsymbol{n}$ is the unit normal vector to the boundary Γ. With the help of (3.15), we find the boundary condition on the function Φ:

$$(\nabla\Phi - \overline{T}\boldsymbol{e})\cdot\boldsymbol{n}\big|_{\Gamma} = 0.$$

In the numerical simulation based on the averaging approach, we consider the two-dimensional problem of thermovibrational convection in a square cell (plane XZ in figure 1*b*). The main goal of two-dimensional simulation is to investigate the system behaviour in a wide range of control parameters (vibrational impact, residual-gravity levels and the like). A detailed analysis of particular experimental runs will be performed on the basis of full equations (3.2), which require much larger computational costs.

In the two-dimensional model, the boundary conditions for the averaged velocity and temperature coincide with (3.5) and (3.6). Taking the same scaling for averaged fields as for their non-averaged counterparts (see § 3.1), we introduce the dimensionless velocity $\overline{\boldsymbol{v}}$, temperature $\overline{\Theta}$, pressure $\overline{p}$ and the function $\varphi = \Phi(\Delta T L)^{-1}$. The averaged equations will be solved in terms of stream function ψ and vorticity ζ, which are introduced by the formulas

$$\overline{\boldsymbol{v}} = (u, w) = \left(\frac{\partial\psi}{\partial z}, -\frac{\partial\psi}{\partial x}\right), \qquad \zeta = \frac{\partial w}{\partial x} - \frac{\partial u}{\partial z}.$$

The governing equations (3.14) are rewritten in the form

$$\left.\begin{aligned}
&\frac{\partial\zeta}{\partial t}+\frac{\partial\psi}{\partial z}\frac{\partial\zeta}{\partial x}-\frac{\partial\psi}{\partial x}\frac{\partial\zeta}{\partial z}=\nabla^2\zeta+\frac{1}{Pr}\left[Ra_x\frac{\partial\overline{\Theta}}{\partial z}-Ra_z\frac{\partial\overline{\Theta}}{\partial x}+Gs\left(\frac{\partial\overline{\Theta}}{\partial z}\frac{\partial^2\varphi}{\partial x^2}-\frac{\partial\overline{\Theta}}{\partial x}\frac{\partial^2\varphi}{\partial x\partial z}\right)\right],\\
&\frac{\partial\overline{\Theta}}{\partial t}+\frac{\partial\psi}{\partial z}\frac{\partial\overline{\Theta}}{\partial x}-\frac{\partial\psi}{\partial x}\frac{\partial\overline{\Theta}}{\partial z}=\frac{1}{Pr}\nabla^2\overline{\Theta},\\
&\nabla^2\varphi=\frac{\partial\overline{\Theta}}{\partial x},\\
&\nabla^2\psi=-\zeta.
\end{aligned}\right\}\tag{3.19}$$

The boundary conditions of the problem are written as

$$\left.\begin{aligned}
x=0,1:\quad &\psi=\frac{\partial\psi}{\partial x}=0, \quad \overline{\Theta}=z, \quad \frac{\partial\varphi}{\partial x}=\overline{\Theta},\\
z=0,1:\quad &\psi=\frac{\partial\psi}{\partial z}=0, \quad \overline{\Theta}=0,1, \quad \frac{\partial\varphi}{\partial z}=0,
\end{aligned}\right\}\tag{3.20}$$

while the initial conditions have the form

$$t=0:\quad \psi=\zeta=0, \quad \overline{\Theta}=z, \quad \frac{\partial\varphi}{\partial x}=\overline{\Theta}, \quad \frac{\partial\varphi}{\partial z}=0. \tag{3.21}$$

The last two conditions follow from (3.15), where the amplitude of oscillatory velocity component $\boldsymbol{W}=0$ at the initial moment of time.

Equations (3.19) include the Rayleigh numbers Ra_x and Ra_z, which are given by (3.4) and characterize the gravitational mechanism of convection (in numerical simulation with averaged equations, we consider only constant gravity levels). The dimensionless parameter Gs is known as their vibrational analogue,

$$Gs=\frac{(A\omega\beta_T\Delta TL)^2}{2\nu\chi}, \tag{3.22}$$

and describes the vibrational mechanism of convection represented by the mean flow. It can be regarded as the ratio of mean vibrational buoyancy force to the product of momentum and thermal diffusivities. Following Naumann (2002), we suggest calling it the Gershuni number (instead of the vibrational Rayleigh number) to mark a significant contribution of G. Z. Gershuni to the theory of thermovibrational convection (Gershuni & Lyubimov 1998). The Gershuni number is related to the oscillatory Rayleigh number Ra_{os} and dimensionless frequency Ω (see (3.4)) by the formula

$$Gs=\frac{1}{2Pr}\left(\frac{Ra_{os}}{\Omega}\right)^2.$$

The relative importance of the vibrational and gravitational convective mechanisms is characterized by the ratios

$$\frac{Gs}{Ra_{x,y,z}}=\frac{(A\omega)^2\beta_T\Delta T}{2g_{x,y,z}L}. \tag{3.23}$$

Here we also included the gravity level in the Y-direction, which is relevant when three-dimensional equations (3.14) are considered. For successful observation of the thermovibrational convection, the vibrational impact should be strong enough to

Mesh size $[n_x \times n_z]$	Nu	$\Psi/n_x n_z$
51×51	2.397	0.024109
76×76	2.435	0.024276
101×101	2.445	0.024308

TABLE 3. The Nusselt number and the normalized sum of the stream function values.

suppress the influence of residual gravity. It follows that the vibrational velocity $A\omega$, the thermal expansion β_T and the applied temperature difference ΔT should be large, while the cell size L and residual-gravity levels $g_{x,y,z}$ should be small.

To investigate the dynamics of transient process, we introduce an integral characteristic based on the instantaneous velocity field. This characteristic is the sum of discrete stream function values over all grid nodes,

$$\Psi(t) = \sum_{i,k} \psi_{ik}, \tag{3.24}$$

which is proportional to the total angular momentum of the fluid in the considered system.

Problem (3.19)–(3.21) is solved by a finite-difference method using a regular equally spaced mesh. The time derivatives are forward differenced, and the convective and diffusive terms are central approximated. The Poisson equations for the stream function ψ and the amplitude of the 'fast' pressure φ (see (3.17)) are solved by introducing an artificial iterative term, which is analogous to the time-derivative one. The ADI method is used to solve the time-dependent problem for the stream function, vorticity and temperature and the amplitude of the fast pressure φ. More details about the numerical procedure can be found in Gaponenko *et al.* (2006).

The accuracy of the numerical method was studied by conducting simulations with different mesh sizes for the same values of parameters as in three-dimensional case (see § 3.1.1). The Nusselt number and the normalized sum of stream function values were used as control parameters. Their values, which correspond to the steady state in terms of mean fields, are given in table 3. Based on these results, the mesh $[76 \times 76]$ was finally chosen for calculations. The dimensionless time step was 10^{-5}. Calculations with smaller time steps did not provide any significant change of control parameters.

4. Impact of residual gravity on heat transfer and mean flow pattern

It was mentioned in the Introduction that a large number of previous theoretical studies were focused on the mean flow organization and its stability. Gershuni & Lyubimov (1998) showed that in a rectangular cavity under weightlessness, a non-zero mean flow exists at any value of the Gershuni number Gs when the direction of vibration is perpendicular to the temperature gradient (this configuration is considered in the present study). For small values of the Gershuni number, the stationary mean flow is weak and has a four-vortex symmetrical structure (see figure 5, left). Such 'quadruple' flows were also observed by Farooq & Homsy (1994) and Savino *et al.* (1998). When the Gershuni number exceeds some critical value Gs_{cr}, a flow pattern bifurcates to the pattern with different symmetry: one large diagonal vortex and two small vortices in the corners (it will be referred to as the three-vortex regime; see figure 5, right). The critical value of the Gershuni number depends on the physical properties of the fluid and boundary conditions. According to Gershuni &

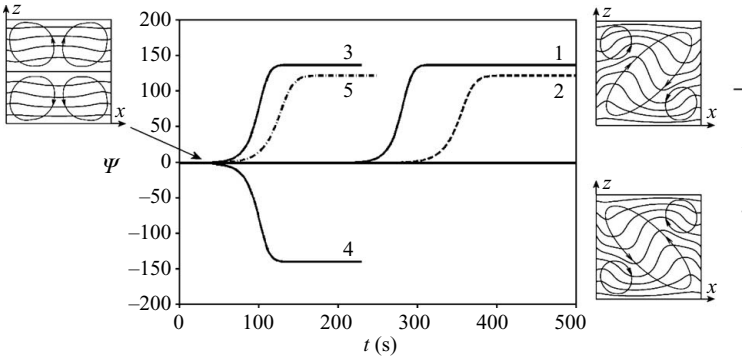

	g_x/g_0	g_z/g_0
1	0	0
2	0	10^{-2}
3	10^{-6}	0
4	-10^{-6}	0
5	-10^{-6}	10^{-2}

FIGURE 5. The evolution of the sum of stream function values for different levels of residual gravity and related flow patterns (a few streamlines and temperature isolines are shown), $Gs = 71.15 \times 10^3$.

Lyubimov (1998), $Gs_{cr} = 8 \times 10^3$ for adiabatic walls and $Gs_{cr} = 15 \times 10^3$ for perfectly conducting walls. The former critical value does not depend on the Prandtl number, while the latter one corresponds to $Pr = 1$. It should be noted that for $Gs > Gs_{cr}$, the four-vortex regime temporally exists as a metastable one. Transition from this regime to the stable diagonal vortex flow occurs after some period of time, which depends on the values of Pr, Gs, $Ra_{x,y,z}$ and boundary conditions.

During the preparation of microgravity experiment on thermovibrational convection and post-flight analysis of the obtained results, we have performed complementary numerical modelling of this phenomenon. The goal of the current study is to understand what kind of mean flow regimes can be observed during the short experimental time of 22 s and assess the influence of residual gravity on the transient process. It should be emphasized that we are interested in mean flows, which can induce heat transfer in a system subjected to external vibration. In this section, the simulations are performed for a square cavity by using averaged equations (3.19), boundary conditions (3.20) and initial conditions (3.21) (the latter approximately correspond to the beginning of microgravity time). The control parameters of the system including the physical properties of the liquid are listed in table 1. In the present study, the temperature difference is fixed at $\Delta T = 20$ K. Under these conditions, the following can be stated: In the considered system (isopropanol in a cubic cell), the Rayleigh numbers $Ra_{x,y,z}$ are determined by the residual-gravity level,

$$Ra_{x,y,z} = \frac{g_{x,y,z}\beta_T \Delta T L^3}{\nu\chi} = 2.492 \times 10^5\, g_{x,y,z}/g_0, \tag{4.1}$$

while the Gershuni number Gs is varied by changing the vibrational velocity $A\Omega$.

The characteristic viscous and thermal times of our system are $\tau_{vs} = 14.5$ s and $\tau_{th} = 401.3$ s, respectively. It makes possible to observe the transient development of the thermovibrational flow and its influence on the thermal field during 22 s of microgravity. In the experiment, we do not study stationary states, since the thermal time is significantly larger than microgravity time.

First, we have investigated the transient process in a system with vibration $f = 4$ Hz, $A = 45$ mm and $\Delta T = 20$ K ($Gs = 71.15 \times 10^3$) for different levels of residual gravity. These parameters correspond to one of the experimental cases of study (see § 5). The evolution of the sum of stream function values (see (3.24)) is presented in figure 5. When Ψ is close to zero, the flow is represented by a four-vortex symmetrical

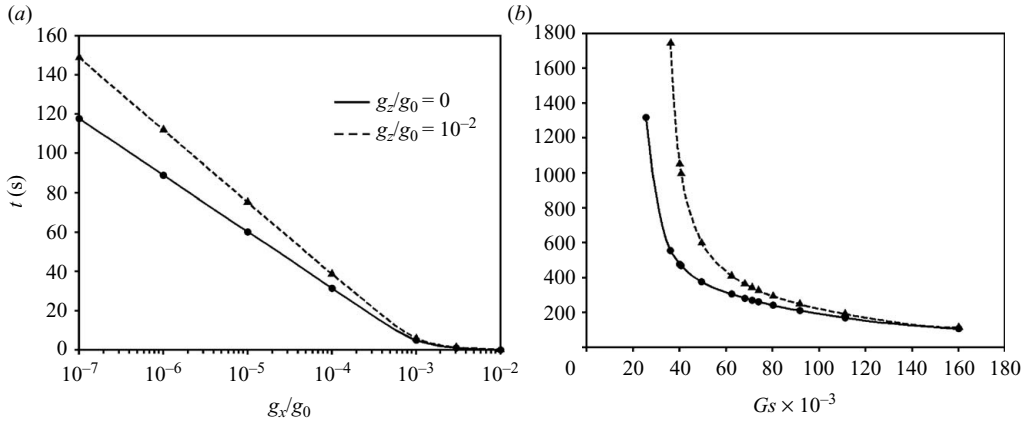

FIGURE 6. (*a*) The lifetime of the four-vortex regime versus the gravity level g_x/g_0 for $Gs = 71.15 \times 10^3$; (*b*) the lifetime of the four-vortex regime versus the Gershuni number, $g_x/g_0 = 0$.

structure. After some time, Ψ deviates from zero and starts to grow (by absolute value) until the steady state is reached (in terms of mean fields). The growth of Ψ is associated with the transition to the flow pattern with three vortices. Visual observations show that this pattern sets in when

$$\frac{\Psi(t)}{\Psi_s} > 0.25,$$

where $\Psi_s = \Psi(\infty)$ is the steady-state value. Based on this criteria, one can define the lifetime of the four-vortex regime as a time during which $\Psi(t)/\Psi_s < 0.25$.

Curve 1 in figure 5 corresponds to the pure weightlessness. The residual gravity in the Z-direction can destabilize (stabilize) the flow when the gravity vector and the temperature gradient have the same (opposite) directions (the temperature gradient is always co-directed with the Z-axis). Curve 2 reflects the stabilizing action of gravity, which delays the transition to the flow structure with three vortices. The lateral residual gravity (in the X-direction) is always destabilizing. It can be seen from figure 5 that even the small gravity level of $g_x/g_0 = 10^{-6}$ can significantly reduce the lifetime of the metastable four-vortex regime (Curve 3). In this case, the ratio of the Gershuni and Rayleigh numbers, which describes the relative importance of vibrational and gravitational convection, is very large: $Gs/Ra_x = 2.855 \times 10^5$. The sign of g_x controls the inclination of the diagonal vortex and the direction of rotation in the steady state (see curves 3 and 4). The joint action of destabilizing g_x and stabilizing $g_z/g_0 = 10^{-2}$ is represented by curve 5. Here one has $Gs/Ra_z = 28.55$.

The dependence of the lifetime of the four-vortex regime on the gravity level g_x/g_0 is presented in figure 6(*a*). The numerical values corresponding to the points in this plot are collected in table 4. It can be seen that the lifetime rapidly decreases with increasing g_x/g_0. When the latter is varied from 10^{-7} to 10^{-2}, the ratio Gs/Ra_x is changing from 2.855×10^6 to 28.55. The stabilizing action of g_z increases the lifetime in comparison with the case in which it is absent. However, the influence of g_z becomes weak with the growth of g_x. Figure 6(*b*) presents the dependence of the lifetime on the Gershuni number. When Gs is increased, the flow regime with three vortices is established faster; so the lifetime of the metastable four-vortex flow decreases. The stabilizing action of g_z delays the transition to the former flow pattern.

$g_x/g_0 =$	0	10^{-7}	10^{-6}	10^{-5}	10^{-4}	10^{-3}	3×10^{-3}	10^{-2}
$g_x/g_0 = 0$	271.3	117.8	88.9	60.0	31.3	5.02	1.05	0.10
$g_z/g_0 = 10^{-2}$	342.3	148.8	112.0	75.1	38.6	5.85	1.18	0.13

TABLE 4. The lifetime (in seconds) of the four-vortex regime for different levels of residual gravity, $Gs = 71.15\times10^3$. See figure 6(*a*) for a graphical representation of the data.

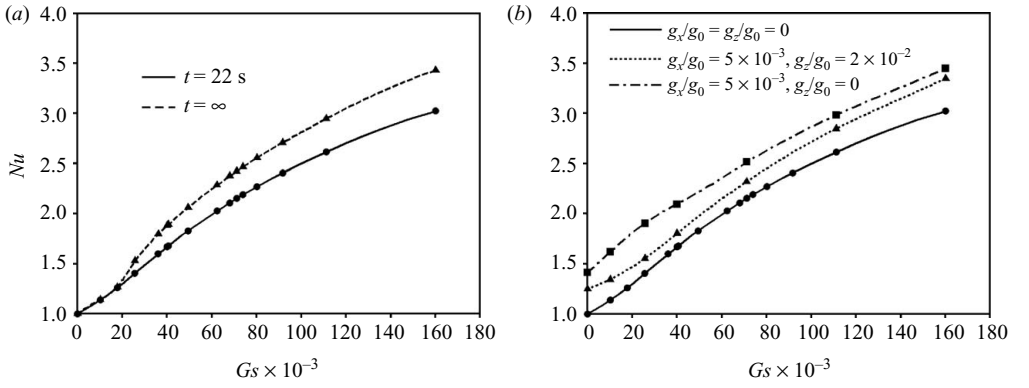

FIGURE 7. (*a*) The Nusselt number versus the Gershuni number at $t = 22$ s from the start of vibration (solid line) and at the steady state (dotted line) for $g_x = g_z = 0$. (*b*) The Nusselt number versus the Gershuni number for different levels of residual gravity at $t = 22$ s.

The performed study shows that in the conditions of parabolic flight, where $|g_x/g_0| \leqslant 10^{-2}$, $|g_z/g_0| \leqslant 5\times10^{-2}$, the expected flow structure is one big diagonal vortex with two small vortices in the corners (in the considered range of the Gershuni numbers). As for the four-vortex flow, it might be observed during the first second after the start of vibration.

We have also investigated the influence of vibration on heat transfer in the system. Figure 7(*a*) shows the dependence of the Nusselt number on the Gershuni number after 22 s from the start of vibration and at the steady state (in weightlessness). The two curves have the same tendency, and the difference between them is not large. It follows that for the considered system, the limited microgravity time is sufficient for observing essential changes in the heat transfer regime because of vibrational convection. It should be noted that the two curves coincide in the range $0 < Gs < Gs_{cr}$, where $Gs_{cr} \approx 18\times10^3$. For these values of the Gershuni number, the flow is represented by a four-vortex pattern, which is established rapidly (within 22 s). For $Gs > Gs_{cr}$, we have a bifurcation to the three-vortex flow regime with a larger transient time. This regime is observed in the steady state for all the Gershuni numbers in the range $Gs_{cr} < Gs < 160\times10^3$. The flow pattern at 22 s from the start of vibration is represented by four vortices for all the Gershuni numbers considered, since its lifetime in weightlessness is large (see table 4). The obtained dependence of *Nu* on *Gs* in the steady state completely agrees with the previous results of Gershuni & Lyubimov (1998). However, the critical value $Gs_{cr} \approx 18\times10^3$ is slightly larger than 15×10^3, which was reported by the above-mentioned authors for $Pr = 1$. It should be noted that in our case $Pr = 27.8$. In a more viscous (or less heat diffusive) fluid, the four-vortex flow can exist for larger values of *Gs*, i.e. for larger vibrational velocities or the applied temperature differences.

The influence of residual gravity on heat transfer in the system is shown in figure 7(*b*). These data correspond to $t = 22$ s from the start of vibration. The presence of constant gravity g_x leads to the increase of the Nusselt number by approximately 0.4. The stabilizing action of g_z compensates this effect, reducing the above-given difference by a factor of 1.5–2. The Rayleigh numbers (see (4.1)), which correspond to the gravity level of figure 7(*b*, dashed line), are given by $Ra_x = 1246$ and $Ra_z = 4983$. Analysing the ratios of the Gershuni number to the Rayleigh numbers with increasing *Gs*, one can determine when vibrational convection starts to dominate the gravitational one. For example, for $Gs = 30 \times 10^3$ one has $Gs/Ra_x = 24$ and $Gs/Ra_z = 6$; so the vibrational convective transport is stronger than the gravitational one. It should be noted that when residual gravity is taken into account, the flow structure at 22 s is represented by three vortices, while in weightlessness one has a four-vortex flow.

It follows from the obtained results that the residual gravity in a parabolic flight affects the heat transfer in the system. Nevertheless, the general trend in the dependence of the Nusselt number on the Gershuni number remains the same as in weightlessness.

5. Discussion of experimental and numerical results

In this section, we present experimental results and compare them with numerical simulations.

We have performed a large number of experimental runs with frequencies and amplitudes in the ranges 1–12 Hz and 10–140 mm, respectively. Most of the results relate to the high-frequency limit (see § 3.2). Two applied temperature differences, namely 15 K and 20 K, were considered. In the experiments, the Gershuni number was varying from 0 to 71×10^3. To study the evolution of the mean flow, one snapshot of the temperature field per period is recorded in the same phase of oscillation (when the interferometric patterns are in the focus of the camera). It should be noted that the preliminary numerical simulations by Melnikov *et al.* (2008) showed that the amplitude of temperature oscillations is very small (or even negligible) with respect to the time-averaged distortion of the thermal field induced by the mean flow. So, one can easily follow the evolution of the mean temperature field by recording one snapshot per period.

For the numerical modelling of thermovibrational convection in real parabolic flight conditions with variable gravity, we use full three-dimensional equations (3.2), boundary conditions (3.5) and (3.6) and initial conditions (3.7). The calculations start 6 min before the series of parabolas (when the aircraft performs horizontal flight). By this time, the temperature profile is already established in the cell (this profile is close to linear). Numerical simulation continues during several parabolas (including the time between them) with a real microgravity profile $\boldsymbol{g}(t)$. The gravity data are taken from measurements of the on-board accelerometer (see figure 3).

5.1. *Intensity of thermovibrational convection and transient behaviour*

The summary of experimental runs, for which three-dimensional numerical simulations were performed, is presented in table 5. In each run, thermovibrational flow develops during 22 s of microgravity. Figure 8 presents a comparison between experimental and numerical flow structures at the end of microgravity time for different Gershuni numbers. The experimental pictures (figure 8*a*) show the projection of the temperature field on the side view plane XZ. The results of direct numerical simulation allow us to calculate the mean velocity and temperature fields according

Run	f (Hz)	A (mm)	ΔT (K)	Ra_{os}	Ω	Gs	$Gs/Ra_{x,y}$	Gs/Ra_z
1	0	0	20	0	0	0	0	0
2	4	20	20	321×10^3	363	14.05×10^3	5.64	2.82
3	8	17	20	1091×10^3	726	40.62×10^3	16.30	8.15
4	4	45	20	722×10^3	363	71.15×10^3	28.55	14.28

TABLE 5. Parameters of several experimental runs, for which three-dimensional numerical simulations with real microgravity profile were performed. In this table, $Ra_{x,y} = 2492$ and $Ra_z = 4983$, which correspond to the typical microgravity level $g_{x,y} = 0.01 g_0$ and $g_z = 0.02 g_0$.

to (3.10). To construct two-dimensional plots (figure 8*b*), the three-dimensional mean temperature field is averaged in the Y-direction; the velocity field is taken at the midplane $Y = 2.5$ mm.

Let us first consider the case in which no vibration is applied (run 1 with $Gs = 0$). The experimental temperature field shows some deviations from a purely conductive state. These deviations result from weak convective flow caused by the residual gravity. The residual accelerations in the X and Y directions (perpendicular to the thermal gradient) slightly destabilize the conductive state (or mean flows when vibration is applied), while their influence in the Z-direction is stabilizing or destabilizing depending on the sign of g_z. According to the results of numerical simulation, convective flow has a one-vortex structure. Comparison between the experimental and numerical temperature fields shows that they are similar in the core region of the cell but exhibit some differences near the sidewalls. In the experiment, the presence of two glass prisms at the sidewalls enhances the heat fluxes through them. In the numerical simulation with linear temperature profile at the walls (see (3.6)), these fluxes are somewhat weaker. In general, we found a very good agreement between experiment and numerical modelling. The analysis of different runs without vibration shows that the deviations from the conductive state are not large.

When vibration is applied to the system, the thermal field undergoes essential changes. For small vibrational contribution of $Gs = 14.05 \times 10^3$ (run 2), the effect is not very strong because of the interaction of vibrational and gravitational convective mechanisms. The ratios $Gs / Ra_{x,y,z}$, which describe the relative importance of these mechanisms, are not large (see table 5). The observed flow pattern is represented by the one vortex, which is inclined to the right. This inclination is associated with positive residual gravity g_x/g_0 during the experimental run (see figures 3 and 8).

With increasing the Gershuni number, thermovibrational convection becomes more intensive and leads to the strong distortion of the thermal field; see run 3 with $Gs = 40.62 \times 10^3$. This effect becomes even more pronounced in run 4 with $Gs = 71.15 \times 10^3$. In the latter case, the ratios $Gs / Ra_{x,y,z}$ are rather large (see table 5); so the vibrational convective mechanism dominates the gravitational one. We found a very good agreement between the experimental and numerical temperature fields. Numerical modelling reveals a flow structure with one big diagonal vortex and two small vortices, which is typical for the above-given values of the Gershuni number.

The development of vibrational convection during experimental run 4 with $Gs = 71.15 \times 10^3$ is shown in figure 9. Initially (0 s), the thermal field is close to the conductive state with a very weak convection due to residual gravity. The thermovibrational flow causes the distortion of the temperature field, which is growing with time. The numerical snapshot taken at 1 s from the start of vibration reveals the

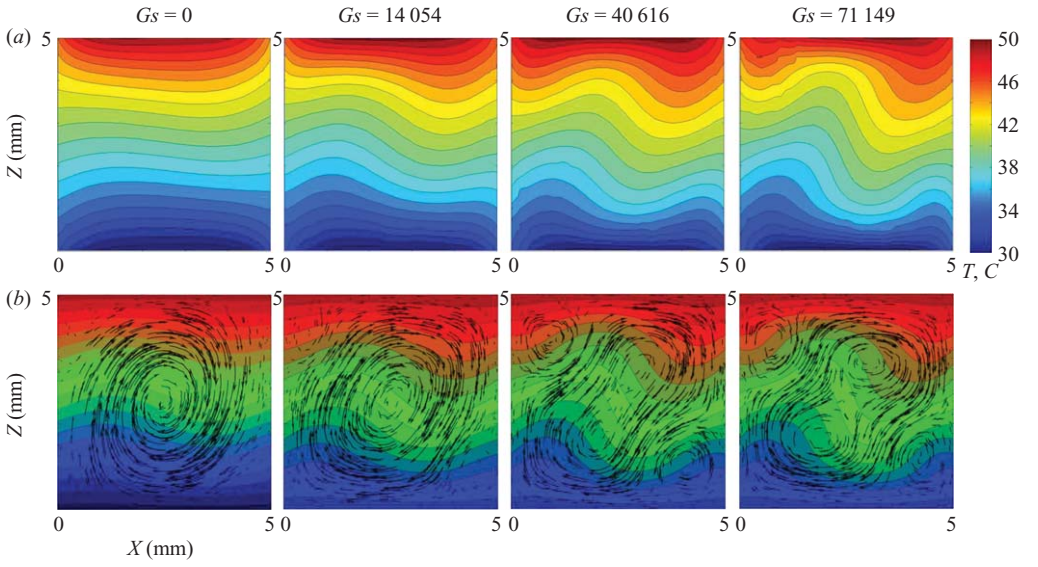

FIGURE 8. Intensity of thermovibrational convection for different Gershuni numbers: comparison between (*a*) experiment and (*b*) numerical simulation. The snapshots are taken at the end of experimental run.

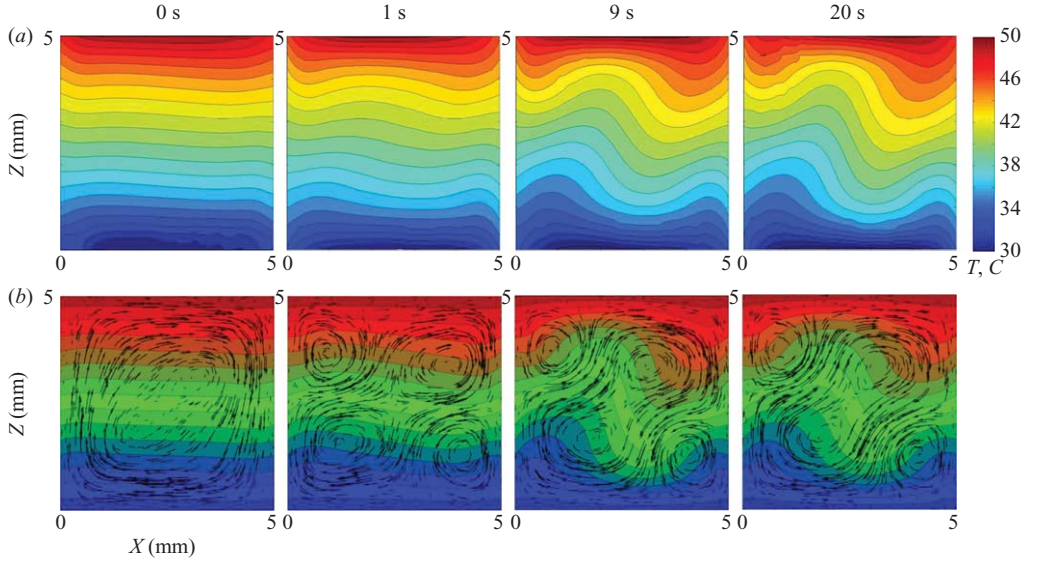

FIGURE 9. The evolution of temperature and velocity fields in the side view during the run with $f = 4$ Hz, $A = 45$ mm, $\Delta T = 20$ K, $Gs = 71149$. Comparison between (*a*) experiment and (*a*) numerical simulation.

mean flow structure with four vortices. The experimental thermal field also indicates the presence of this structure. The flow is not completely symmetrical because of the presence of residual gravity. This result is consistent with the predictions of two-dimensional numerical modelling in § 4, where it was stated that for the constant gravity level of $g_x/g_0 = 3 \times 10^{-3}$ and $g_z/g_0 = 10^{-2}$, the four-vortex regime exists during

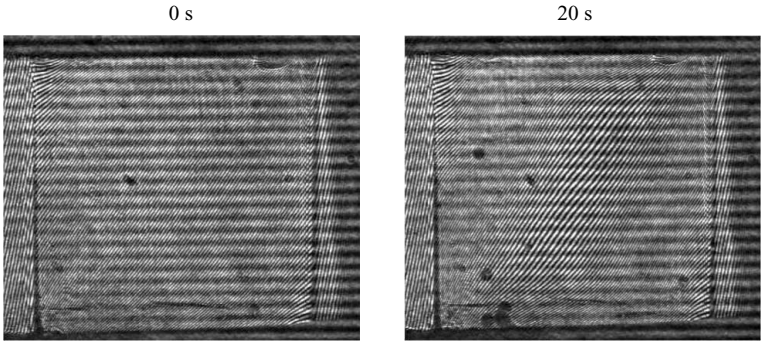

FIGURE 10. Interference patterns of the side view of the cell at different times, $f = 4$ Hz, $A = 45$ mm, $\Delta T = 20$ K, $Gs = 71.15 \times 10^3$.

1.18 s (see table 4). After the first second, it bifurcates to the pattern with one big diagonal vortex and two small vortices in the corners (9 and 20 s). The comparison between the experimental temperature fields at 9 and 20 s reveals a slight increase in the inclination of isotherms in the core region of the cell, while numerical modelling shows some decrease. However, this effect is of minor importance, and the agreement between experiment and numerical simulation is very good.

Figure 10 presents the interference patterns of the cell at 0 and 20 s from the start of vibration. The corresponding thermal fields in figure 9 were restored from these patterns. In the first frame (0 s), the pattern is formed by the interchange of the thin black and white lines (fringes). These lines are inclined and almost parallel; in addition, they have the same thickness except for the regions near the lateral walls, where temperature slightly deviates from purely conductive state. In the second frame (20 s), we see that the thickness of fringes increases in the diagonal from the bottom left to the top right corner (see also figure 2*a*). Around this diagonal, the thickness decreases. In addition, the deformation of fringes becomes larger. All these changes result from the deformation of the temperature field by thermovibrational convection.

The experimentally observed flow regimes including the transition from four-vortex to three-vortex pattern confirm the previous numerical studies of Gershuni & Lyubimov (1998), Gershuni *et al.* (1982) and Savino & Monti (1998, 2001). The results of two-dimensional simulations (§ 4) suggest that the three-vortex pattern observed at the end of microgravity time is close to the stable configuration, to which the system would arrive in a long-duration experiment. The intensity of flow can slightly increase on the way to the steady state (see figure 7*a*), but the mean flow structure will remain the same.

It should be noted that the vibrational mean flow structures observed in the current work are somewhat similar to those induced by the static gravity (see, for example, the work of Pallares *et al.* (2001) on Rayleigh–Bénard convection in a cubic cavity). This fact supports the idea of employing vibrations for creating 'artificial gravity' in space (Beysens 2006) in order to transport fluids and heat.

5.2. *Three-dimensional flow structure*

To study the spatial flow structure, we refer to the experimental measurements, which provide the projections of the temperature field on two perpendicular planes, and numerical modelling. A comparison between experimental and numerical results is presented in figure 11. The thermal patterns in the front and side views (planes YZ and XZ, respectively) are shown at the end of experimental run 4 with $Gs = 71.15 \times 10^3$.

The numerical patterns are obtained by averaging in the X and Y directions for the front and side views, respectively. One can see that the side view patterns in experiment and numerical modelling are practically identical. The same is true for the front view patterns in the core region of the cell. However, the structure of isotherms near the lateral walls shows some differences between experiment and numerical simulation. In general, the distortion of the thermal field in the front view is much less than in the side view. It can be explained by the fact that the flow is developing in the XZ plane formed by the directions of vibration and the temperature gradient. The temperature field in the front view is a superposition of patterns in the planes of constant X. Because of the specific structure of the side view pattern, an interchange of higher- and lower-temperature regions occurs when one moves in the X-direction at fixed Y and Z. It explains the obtained front view pattern. Analysing its transient behaviour, we found that the distance between isotherms in the central part of the cell is slightly increasing with time, while near the top and bottom walls isotherms are approaching each other.

To investigate three-dimensional velocity field, numerical and experimental particle tracing has been performed. First, we analyse the trajectories of 'numerical' fluid particles (in other words, the structure of streamlines) to visualize the three-dimensional flow field. For numerical modelling of a fluid particle motion, one should solve the problem

$$\frac{\mathrm{d}\boldsymbol{R}}{\mathrm{d}t} = \boldsymbol{V}(\boldsymbol{R}, t), \qquad \boldsymbol{R}(0) = \boldsymbol{R}_0, \tag{5.1}$$

where $\boldsymbol{V}$, $\boldsymbol{R}$, $\boldsymbol{R}_0$ are the dimensional velocity, current position and initial position of a fluid particle, respectively. The velocity is obtained by solving the governing equations (3.1). The integration of (5.1) is performed by using the fourth-order Runge–Kutta method and linear interpolation of velocity from the grid nodes into the particle's current position. This approach was proven to be accurate (see Melnikov & Shevtsova 2005).

Figure 12 shows the three-dimensional flow structure. To obtain this picture, we placed 100 equally spaced particles (10×10) in each of the planes $X = 0.5$ mm and $X = 4.5$ mm and followed their trajectories during the experimental run (22 s) by integrating (5.1). The mean flow pattern consisting of one big diagonal vortex and two small vortices in the corners (shown by red and blue) is clearly seen. It should be noted that during the first second, the mean flow pattern was represented by four vortices (see figure 9*b*). However, the contribution of this regime to the structure of particle trajectories shown in figure 12 is negligible because of its small lifetime.

The three-dimensional flow field reveals that the motion in the Y-direction is rather weak. The flow patterns in the planes of constant Y are similar (except small regions near the side walls); so the mean flow can be described as quasi two-dimensional. The oscillation amplitude of a given particle depends on its current position in the cell. In the big diagonal vortex, the particles have small amplitudes near the walls. When these particles approach the small vortices (where the amplitude is large) and go round them, the amplitude increases, then decreases, increases again and finally decreases. The present experimental and numerical results confirm the first three-dimensional calculations of vibrational mean flows in a cubic cavity by Savino *et al.* (1998).

To evaluate the velocity of the mean flow, we have compared the evolution of maximum mean velocity in the volume (obtained from numerical simulation) and the mean velocity of the experimental tracer particle, which performs a loop trajectory in figure 11(*a*). The result is presented on figure 13. In this plot, the time moment

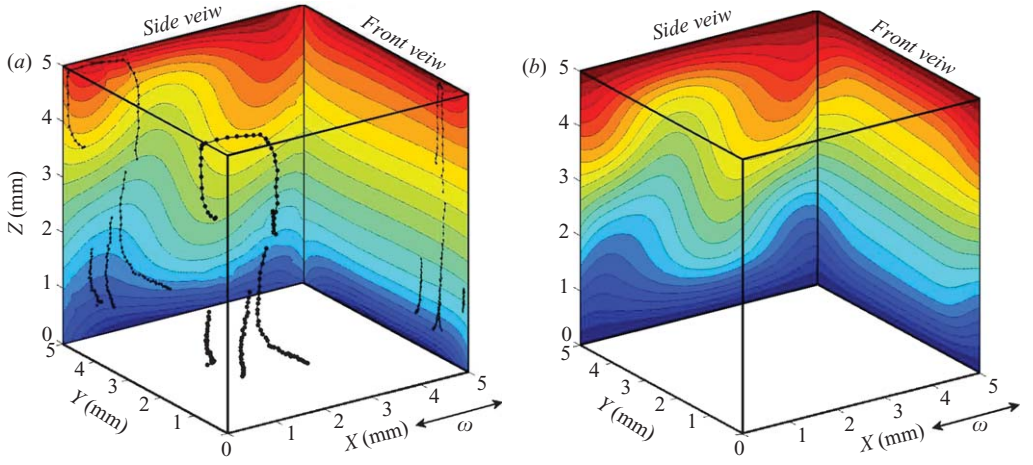

FIGURE 11. Comparison between the (*a*) experimental and (*b*) numerical temperature fields. In the experimental picture, the mean trajectories of several particles are also shown.

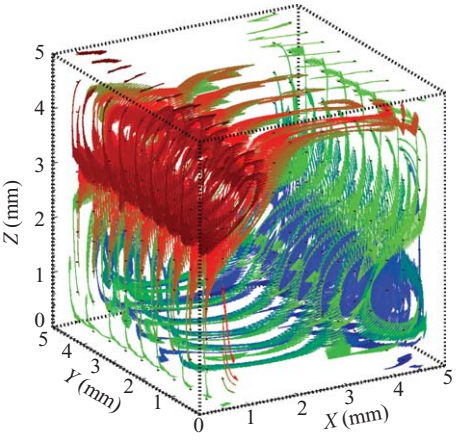

FIGURE 12. The trajectories of fluid particles starting from planes $X = 0.5$ mm and $X = 4.5$ mm (numerical simulation). The particles are moving along the mean flow streamlines while performing oscillatory motion.

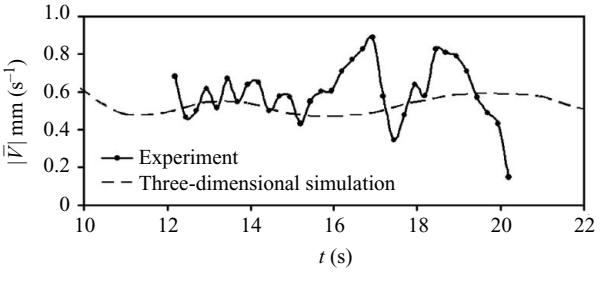

FIGURE 13. The evolution of maximum mean velocity (simulation) and mean velocity of a single experimental fluid particle.

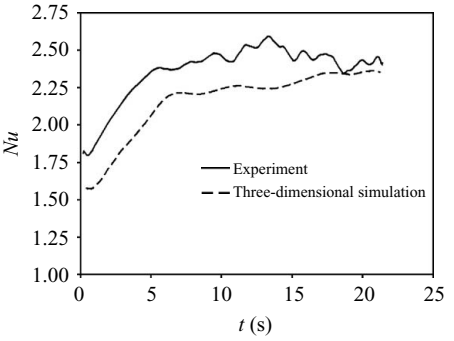

FIGURE 14. The evolution of the Nusselt number with time during the run with $f = 4$ Hz, $A = 45$ mm, $\Delta T = 20$ K, $Gs = 71.15 \times 10^3$. The experimental data and the results of three-dimensional numerical simulation are shown.

$t = 0$ s corresponds to the beginning of microgravity. One can see that the deviation of the experimental curve from the numerical one is rather small for $t = 12$–16 s but becomes larger at the end of the run. In general, the agreement between experiment and simulation is rather good.

5.3. *Enhancement of heat transfer*

The experimental study of thermovibrational convection for different vibrational excitations and applied temperature differences allowed us to measure the influence of vibration on heat transfer in the system quantitatively. To calculate the Nusselt number, polynomial approximation of the experimental temperature field near the walls was used. The normal component of temperature gradient $\partial T/\partial n$ was calculated and summed up over the whole boundary according to (3.8). The evolution of the Nusselt number during experimental run 4 with $Gs = 71.15 \times 10^3$ (see table 5) is shown in figure 14. Heat transfer is increased rapidly during the first 5 s after the start of vibration. Then the growth of the Nusselt number is slowed down, and during the last 5 s of microgravity time this number slightly decreases, showing some oscillations. The results of three-dimensional numerical modelling are also shown in the same plot. For a correct comparison with experimental measurements, the three-dimensional temperature field is averaged in the Y-direction, and then the Nusselt number is calculated according to (3.8). One can see that there is some difference between experimental and numerical curves. We attribute this difference to the heat fluxes through the lateral walls, which are formed by two glass prisms in the experimental set-up. It can be seen from figure 8 (case $Gs = 71.15 \times 10^3$) that experimental temperature gradients near the lateral walls and at the corners of the cell are stronger than those predicted by numerical modelling (where a linear temperature profile on the lateral walls is imposed). Nevertheless, the general trend in the growth of the Nusselt number is the same in theory and experiment. The numerical and experimental values are rather close at the end of microgravity time. Apparently, the agreement between experiment and simulation can be made even better by taking into account heat transfer in the lateral walls. However, our goal is not to stay as close as possible to a particular experimental set-up with its complex geometry (such as the rhombic shape of the walls). The main advantage of the present study is that we have found a good agreement between experiment and simulation by using simple boundary conditions employed in many previous theoretical works.

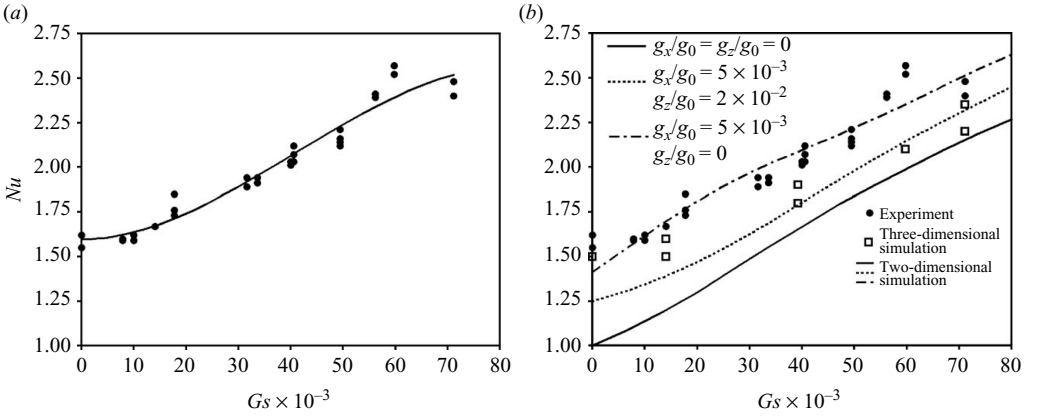

FIGURE 15. (*a*) The experimental dependence of the Nusselt number on the Gershuni number. (*b*) The dependence of the Nusselt number on the Gershuni number. The experimental data and the results of two-dimensional and three-dimensional numerical simulations are shown.

The experimental dependence of the Nusselt number on the Gershuni number is presented in figure 15(*a*). The Nusselt number is calculated by taking the average value of $Nu(t)$ over the last 3 s of the experimental run. The solid curve outlines the tendency in the dependence of Nu on Gs. For small Gershuni numbers ($Gs \lesssim 15 \times 10^3$), the Nusselt number is around 1.6 and does not depend on the level of vibration. In this region, the situation is controlled by the residual gravity, which produces relatively weak convective flows (see also figure 8). With increasing the Gershuni number, the thermovibrational effect starts to dominate the gravitational one, and the Nusselt number increases significantly. It should be noted that the scattering of experimental points is rather small, and the trend is clearly seen.

The comparison between experimental measurements and the results of two-dimensional and three-dimensional numerical modelling is presented in figure 15(*b*). The continuous lines correspond to two-dimensional studies, which are based on the averaging approach (see also figure 7*b*). The results of three-dimensional simulations on the basis of full-nonlinear equations are shown by the open squares (different squares for the same values of Gs correspond to the parabolas with slightly different residual-gravity profiles). It can be seen that experimental values are slightly larger than their numerical counterparts. These values are distributed along the line corresponding to the constant gravity level of $g_x/g_0 = 5 \times 10^{-3}$, $g_z/g_0 = 0$. Note that in real parabolic flight conditions, g_x/g_0 is not constant and varies around the above value, while g_z/g_0 can be positive (stabilizing) or negative (destabilizing) (see figure 3). In addition, it has been already noted that the experimental fluxes through the lateral walls are somewhat stronger than those predicted by numerical simulation. These factors explain some difference between experimental and numerical results. However, it can be seen that experimental data have the same tendency as numerical ones and are simply shifted by a constant value (around 0.45) from the ideal curve corresponding to the zero-gravity environment. We conclude that the agreement between numerical simulation and experiment is rather good. The obtained results clearly demonstrate that vibrational convection strongly intensifies the heat transfer in the system.

We have also performed a number of studies in normal gravity conditions ($g_z/g_0 = 1$). In these experiments, the heating is provided from above; so the

action of gravity is to stabilize the system. It was observed that gravity drastically suppresses thermovibrational convection. The maximum vibrational level available in the experiments ($Gs = 71.15 \times 10^3$) is still rather weak to overcome the action of static gravity ($Gs/Ra_z = 0.29$). The observed thermal field was close to the conductive state without noticeable deformation of isotherms.

6. Conclusions

In the present work, we have performed an extensive experimental and computational study of thermal vibrational convection in a reduced-gravity environment of a parabolic flight ($g \sim 10^{-2} g_0$). The experiments were carried out in a cubic cell with differentially heated walls, which was filled with isopropanol and subjected to translational vibration in the direction perpendicular to the temperature gradient. The main objective was to study time-averaged (mean) flows, which can essentially affect the regime of heat transfer in the fluid. To observe these flows, the temperature field in the side and front views of the cell was measured by optical digital interferometry, while the velocity field was recorded with help of tracer particles. In computational studies of thermovibrational convection, two numerical approaches were employed: (*a*) two-dimensional simulations on the basis of averaged equations describing the mean fields and (*b*) three-dimensional modelling on the basis of full Navier–Stokes and heat transfer equations. Experimental measurements showed that fixed temperatures on the hot and cold walls and linear temperature profile on the other (lateral) walls provide the proper boundary conditions for numerical modelling.

According to the averaged model, the structure of the mean flow in the stationary state is determined by the dimensionless Gershuni number *Gs*, which characterizes the vibrational impact. Two-dimensional numerical modelling in the range $0 \leqslant Gs < 160 \times 10^3$ predicted two flow regimes in zero gravity: symmetrical four-vortex flow when $Gs < Gs_{cr}$ and a flow with one big diagonal vortex and two small vortices in the corners for $Gs > Gs_{cr}$, where $Gs_{cr} \approx 18 \times 10^3$. Above this critical value, the four-vortex regime is metastable, and its lifetime decreases with increasing *Gs*. The influence of residual gravity on the bifurcation process was first investigated. The calculations revealed the growth of the Nusselt number *Nu* (i.e. enhancement of heat transfer) with increasing the Gershuni number. It was also shown that the heat transfer is increased (decreased) by the destabilizing (stabilizing) action of residual gravity.

The experiments performed in parabolic flights provided one of the first quantitative observations of thermal vibrational convection in a reduced-gravity environment. The transient development of vibrational mean flows was observed during a large number of microgravity periods with different level of vibration (each period lasts around 22 s). Measurements of temperature field revealed large deviations from conductive state due to vibrational mean flows. The transition from four-vortex flow to the pattern with one diagonal vortex was observed in the transient state. A very good agreement was found between experimental results and three-dimensional numerical simulations with real microgravity profile recorded by the on-board accelerometer. It was found that the flow is developing in parallel planes formed by the direction of vibration and temperature gradient. The flow patterns in all such planes are similar; so the total flow can be described as quasi-two-dimensional. The numerical modelling of fluid motion confirms the experimentally observed trajectories of tracer particles. The experimental dependence of the Nusselt number on the Gershuni number in the range $0 \leqslant Gs \leqslant 71 \times 10^3$ was obtained. It showed a significant enhancement of heat

transfer with increasing the vibrational impact. For example, vibration of the level $f = 4$ Hz, $A = 45$ mm, $Gs = 71 \times 10^3$ can enhance heat transfer rate by more than 60 % in comparison with the case in which no vibration is applied. The obtained data are in good agreement with two-dimensional and three-dimensional numerical results. Note that in some way, the considered mean flows are similar to acoustic streaming. The fundamental understanding of heat transfer enhancement by streaming is highly important for a wide range of applications from heat exchangers to microchannels and mini-channels. Thus, the results of the present study can be of interest for a large scientific community.

The present experimental and numerical study confirms and essentially extends the previous findings of theoretical origin. It reveals a similarity between vibrational mean flows in weightlessness and gravity-induced convection. This fact suggests that gravity effects on non-uniformly heated fluids can be reproduced in weightlessness by applying vibrations to the system. It provides potential applications to the operation and control of fluids in space.

This work is supported by the PRODEX programme of the Belgian Federal Science Policy Office.

Appendix. On the validity of Boussinesq approximation

Let us consider the general equations describing compressible viscous heat-conducting fluid in the presence of external vibration and the gravity field (Landau & Lifshitz 1987; Tritton 1988):

$$\rho\left(\partial_t \boldsymbol{V} + (\boldsymbol{V}\cdot\nabla)\,\boldsymbol{V}\right) = -\nabla P + \mu\nabla^2\boldsymbol{V} + \left(\lambda + \frac{\mu}{3}\right)\nabla(\nabla\cdot\boldsymbol{V}) + \rho\left(\boldsymbol{g} + A\omega^2\cos(\omega t)\,\boldsymbol{e}\right), \tag{A 1}$$

$$\partial_t\rho + \boldsymbol{V}\cdot\nabla\rho + \rho\nabla\cdot\boldsymbol{V} = 0, \tag{A 2}$$

$$\rho c_p\left(\partial_t T + \boldsymbol{V}\cdot\nabla T\right) - \beta_T(T_0+T)\left(\partial_t P + \boldsymbol{V}\cdot\nabla P\right) = \kappa\nabla^2 T + \frac{\mu}{2}\sum_{i,j=1}^{3}\left(\frac{\partial V_i}{\partial X_j} + \frac{\partial V_j}{\partial X_i} - \frac{2}{3}\,\delta_{ij}\nabla\cdot\boldsymbol{V}\right)^2 + \lambda(\nabla\cdot\boldsymbol{V})^2. \tag{A 3}$$

Here T and P are the deviations of full temperature and pressure from the mean values T_0 and P_0, respectively. Further, μ is the dynamic viscosity; λ is the second viscosity coefficient; c_p is the specific heat capacity; κ is the thermal conductivity; δ_{ij} is the Kronecker delta; and $\boldsymbol{X} = (X_1, X_2, X_3)$ and $\boldsymbol{V} = (V_1, V_2, V_3)$ are the coordinate and velocity vectors, respectively. The gravity vector is assumed to be constant and corresponds to the maximum level of time-dependent gravity along the corresponding axis.

First, let us formulate the basic assumptions of Boussinesq approximation:

(i) The deviations of temperature and pressure from the mean values are small, i.e.

$$|T/T_0| \ll 1, \qquad |P/P_0| \ll 1. \tag{A 4}$$

Then the equation of state can be written as

$$\rho = \rho_0(1 - \beta_T T + \beta_P P).$$

(ii) The density variation with pressure is much smaller than that with temperature, and the latter is also small,

$$|\beta_P P| \ll |\beta_T T| \ll 1. \tag{A 5}$$

(iii) The variation of density with T and P is negligible everywhere except the external force term in (A 1), where the density is written as

$$\rho = \rho_0(1 - \beta_T T). \tag{A 6}$$

(iv) The contribution of viscous energy dissipation and pressure variations to the energy balance (A 3) is negligible.

Under these assumptions, (A 1)–(A 3) are reduced to (3.1). In what follows, we consider the case of 'vibration in zero gravity', i.e. $A\omega \neq 0$, $\boldsymbol{g} = 0$. The case of 'static gravity without vibration' has been extensively addressed in the literature (see, for example, Tritton 1988). If Boussinesq approximation is valid in both cases, then it is also valid when vibration and static gravity are present simultaneously.

In the current work, the attention is restricted to high-frequency vibrations (see § 3.2). Then the velocity and temperature fields can be decomposed into time-averaged part, which satisfies (3.14), and oscillatory part described by (3.17). Using these equations, we can estimate the magnitudes of averaged and oscillatory parts. The criteria for the validity of Boussinesq approximation are derived by introducing these estimations into assumptions (i)–(iv).

First, the averaged temperature is estimated as $|\overline{T}| \sim \Delta T$; so one has $|\boldsymbol{W}| \sim |\Phi| \sim \Delta T$ from (3.15). According to (3.17), the magnitudes of oscillatory fields are given by

$$|\boldsymbol{V}'| \sim \beta_T \Delta T A\omega, \qquad |T'| \sim \beta_T \Delta T^2 A/L, \qquad |P'| \sim \rho_0 \beta_T \Delta T A\omega^2 L. \tag{A 7}$$

The time derivatives of these variables are estimated by differentiating them with respect to the 'fast' time t (note that the functions $\overline{T}$, $\boldsymbol{W}$, Φ do not depend on this time).

To estimate the averaged velocity, we note that for developed flow, the convective or viscous term (or both) should be proportional to the mean vibrational force term in the first equation of (3.14). In addition, these two terms cannot become large in comparison with the external force term, as the latter is the cause of motion.

Let us first suppose that

$$|\nu \nabla^2 \overline{\boldsymbol{V}}| \sim \left| \frac{(\beta_T A\omega)^2}{2} \big((\overline{T}\boldsymbol{e} - \nabla\Phi)\cdot\nabla\big)\nabla\Phi \right|.$$

It gives the following magnitude of the averaged velocity:

$$|\overline{\boldsymbol{V}}| \sim \frac{(\beta_T \Delta T A\omega)^2 L}{\nu}.$$

Comparing the magnitudes of convective and viscous terms, we find

$$\frac{|(\overline{\boldsymbol{V}}\cdot\nabla)\overline{\boldsymbol{V}}|}{|\nu\nabla^2\overline{\boldsymbol{V}}|} \sim \frac{|\overline{\boldsymbol{V}}|L}{\nu} \equiv Re \sim \frac{Gs}{Pr}, \tag{A 8}$$

where Re is the Reynolds number. This estimation is valid for small Reynolds numbers ($Re < 1$). When Re is large, relation (A 8) predicts that the viscous term is much smaller than the convective one. It is in contradiction with the original assumption that the viscous term is comparable to the mean vibrational force term.

Now consider the case in which the convective term is comparable to the external force term. It gives the estimations

$$|\overline{\boldsymbol{V}}| \sim \beta_T \Delta T A\omega, \qquad Re \sim \left(\frac{Gs}{Pr}\right)^{1/2},$$

which are valid for large Reynolds numbers ($Re \geqslant 1$). Note that the above estimation of the averaged velocity coincides with that for the oscillatory one (see (A 7)). However, numerical calculations in a wide range of the Gershuni numbers show that the averaged velocity is much smaller than the oscillatory one. The proportionality factor $\gamma \sim |\overline{V}|/|V'| < 1$ can be obtained from these calculations. For $Re < 1$, we find

$$Re \sim \gamma^2 \frac{Gs}{Pr}, \qquad |\overline{V}| \sim \frac{(\gamma \beta_T \Delta T A \omega)^2 L}{\nu},$$

while for $Re \geqslant 1$,

$$Re \sim \gamma \left(\frac{Gs}{Pr}\right)^{1/2}, \qquad |\overline{V}| \sim \gamma \beta_T \Delta T A \omega.$$

In the present study of thermovibrational convection in a square cavity with $Pr = 27.8$ (isopropanol), we obtain $\gamma = 0.0195$, which corresponds to the maximum averaged velocity.

Assuming that the pressure gradient is comparable to the mean vibrational force term in the first equation of (3.14), we obtain

$$|\overline{P}| \sim \varepsilon \rho_0 (\beta_T \Delta T A \omega)^2.$$

In dimensionless form, this relation is written as $|\overline{p}| \sim \varepsilon\, Gs/Pr$, where ε is the proportionality factor. For the present system, we found $\varepsilon = 0.0792$. It is expected that $0 < \varepsilon < 1$ in a wide range of the Prandtl numbers.

To estimate the time derivatives of averaged components, we note that in the present study, the transfer of heat and mass during the experimental time is mainly due to convection. Thus, the characteristic time can be estimated as the length scale divided by the magnitude of average velocity, i.e. $L/|\overline{V}|$. Note that the results below are also valid for stationary averaged flows.

Let us now introduce the obtained estimations into the basic assumptions of Boussinesq approximation, taking into account (3.3) and (3.9). Assumption (i) (see (A 4)) leads to

$$\frac{\Delta T}{T_0} \ll 1, \qquad \frac{\rho_0 A \omega^2 L}{P_0} \ll 1. \tag{A 9}$$

Note that here and below we present only independent criteria and skip the dependent ones (including those obtained by multiplying the existing criteria by $\gamma < 1$, $\varepsilon < 1$). For example, for the oscillatory temperature component, it follows from (A 4) that

$$\frac{\beta_T \Delta T A}{L} \frac{\Delta T}{T_0} \ll 1,$$

which is satisfied once (3.13) and the first inequality in (A 9) hold.

In the averaging approach, the full governing equations are separated into the equations for averaged and oscillatory fields. Therefore, we require that assumption (ii) (see (A 5)) must be satisfied for averaged and oscillatory components separately (including their time derivatives). It gives the following criteria:

$$\beta_T \Delta T \ll 1, \qquad \beta_P \rho_0 \left(\frac{\omega L}{\beta_T \Delta T}\right)^2 \ll 1. \tag{A 10}$$

Here the second inequality is connected with the requirement that the acoustic wavelength τc (where c is the speed of sound and $\tau = 2\pi/\omega$ is the period of vibration) must be greater than the characteristic length scale L. Taking into account that

$c^2 = \partial p/\partial\rho = (\beta_P \rho_0)^{-1}$, we can rewrite the above requirement as

$$\beta_P \rho_0 (\omega L)^2 \ll 1,$$

This restriction is weaker than the last one in (A 10) as $\beta_T \Delta T \ll 1$.

The conditions, under which assumptions (iii) and (iv) are satisfied, are derived in two steps. First, we substitute representation (3.9) into system (A 1)–(A 3), obtain equations for oscillatory fields and derive the criteria under which these equations are reduced to (3.16). Second, we average the full governing equations over the period, taking into account (3.9) and (3.17) and derive the criteria under which the resulting equations are reduced to (3.14).

One can consider two cases depending on whether the Reynolds number is less or greater than unity (in practice, one should check the value of $\gamma^2 Gs/Pr$):

(*a*) Flows with small Ryenolds number ($Re < 1$). Substituting (A 6) into continuity equation (A 2) and collecting the oscillatory terms gives

$$-\beta_T \left(\partial_t T' + \overline{\boldsymbol{V}} \cdot \nabla T' + \boldsymbol{V}' \cdot \nabla \overline{T} + \boldsymbol{V}' \nabla T' + T' \nabla \cdot \overline{\boldsymbol{V}}\right) + \left(1 - \beta_T \overline{T} - \beta_T T'\right) \nabla \cdot \boldsymbol{V}' = 0.$$

This equation is reduced to $\nabla \cdot \boldsymbol{V}' = 0$ by requiring that all other terms are negligible in comparison with $\nabla \cdot \boldsymbol{V}'$. Further, the oscillatory part of momentum equation (A 1) is reduced to the first equation in (3.16) with the help of assumptions (i) and (ii) in § 3.2 and the criteria derived above. Finally, the reduction of the oscillatory part of energy equation (A 3) to the second equation in (3.16) imposes an additional criterion:

$$\frac{T_0 (\omega L)^2}{c_p \Delta T^2} \ll 1.$$

In this case, all terms were compared with $\boldsymbol{V}' \cdot \nabla \overline{T}$.

Consideration of averaged equations provides an additional restriction:

$$\frac{\nu^2}{\gamma^2 L^2 c_p \Delta T} \ll 1. \tag{A 11}$$

This inequality is derived from the condition that the contribution of viscous energy dissipation due to oscillatory motion to the time-averaged energy balance is negligible in comparison with convective transfer of heat.

(*b*) Flows with large Reynolds number ($Re \geqslant 1$). This case is treated in a similar manner and provides the same criteria except relation (A 11), which should be replaced by

$$\frac{\nu \beta_T A\omega}{\gamma L c_p} \ll 1.$$

To check the validity of Boussinesq approximation, we substitute the physical and control parameters of the present study into the derived criteria. The parameters, which are not listed in table 1, are the following: $T_0 = 313$ K, $P_0 = 101325$ Pa, $c_p = 2735$ J (kg K)$^{-1}$, $\beta_P = 1.02 \times 10^{-9}$ Pa^{-1}. The maximum values of vibrational acceleration and frequency are specified in § 2.1. The maximum vibrational velocity is $A\omega = 1.18$ m s^{-1}, and the maximum gravity level is $g = 1.8 g_0$ m^2 s^{-1}. One can easily check that all the obtained criteria are satisfied for $\Delta T = 20$ K.

REFERENCES

Alexander, J. I. D. 1990 Low gravity experiment sensitivity to residual accelerations: a review. *Microgravity Sci. Technol.* **3**, 52.

Babushkin, I. A., Bogatyrev, G. P., Glukhov, A. F., Putin, A. F., Avdeev, S. V., Ivanov, A. I. & Maksimova, M. M. 2001 Investigation of thermal convection and low-frequency microgravity by the DACON Sensor aboard the MIR orbital complex. *Cosmic Res.* **39** (2), 161.

Babushkin, I. A. & Demin, V. A. 2006 Vibrational convection in the Hele–Shaw cell: theory and experiment. *J. Appl. Mech. Tech. Phys.* **47** (2), 183.

Beysens, D. 2006 Vibrations in space as an artificial gravity? *Europhys. News* **37** (3), 22.

Biringen, S. & Danabasoglu, G. 1990 Computation of convective flow with gravity modulation in rectangular cavities. *J. Thermophys.* **4**, 357.

Chorin, A. J. 1968 Numerical solution of the Navier–Stokes equations. *Math. Comput.* **22**, 745.

Cisse, I., Bardan, G. & Mojtabi, A. 2004 Rayleigh–Bénard convective instability of a fluid under high-frequency vibration. *Intl J. Heat Mass Transfer* **47**, 4101.

Demin, V. A., Gershuni, G. Z. & Verkholantsev, I. V. 1996 Mechanical quasi-equilibrium and thermovibrational convective instability in an inclined fluid layer. *Intl J. Heat Mass Transfer* **39**, 1979.

Farooq, A. & Homsy, G. M. 1994 Streaming flows due to g-jitter-induced natural convection. *J. Fluid Mech.* **271**, 351.

Farooq, A. & Homsy, G. M. 1996 Linear and nonlinear dynamics of a differentially heated slot under gravity modulation. *J. Fluid Mech.* **313**, 38.

Gaponenko, Y. A., Pojman, J. A., Volpert, V. A. & Zenkovskaya, S. M. 2006 Effect of high-frequency vibration on convection in miscible liquids. *J. Appl. Mech. Tech. Phys.* **47** 1, 190.

Garrabos, Y., Beysens, D., Lecoutre, C., Dejoan, A., Polezhaev, V. & Emelianov, V. 2007 Thermoconvectional phenomena induced by vibrations in supercritical SF_6 under weightlessness. *Phys. Rev.* E **75**, 056317.

Gershuni, G. Z., Kolesnikov, A. K., Legros, J. C. & Myznikova, B. I. 1997 On the vibrational convective instability of a horizontal, binary-mixture layer with the Soret effect. *J. Fluid Mech.* **330**, 251.

Gershuni, G. Z. & Lyubimov, D. V. 1998 *Thermal Vibrational Convection.* Wiley.

Gershuni, G. Z., Zhukhovitskii, E. M. & Yurkov, Y. S. 1982 Vibrational thermal convection in a rectangular cavity. *Fluid Dyn.* **17** (4), 565.

Hirata, K., Sasaki, T. & Tanigawa, H. 2001 Vibrational effects on convection in a square cavity at zero gravity. *J. Fluid Mech.* **445**, 327.

Ishikawa, M. & Kamei, S. 1993 Instabilities of natural convection induced by gravity modulation. *Microgravity Sci. Technol.* **6** (4), 252.

Ivanova, A. A. & Kozlov, V. G. 2003 Thermal vibrational convection in a cavity under nontranslational oscillations. *Fluid Dyn.* **38** (3), 372.

Landau, L. D. & Lifshitz, E. M. 1987 *Fluid Mechanics.* Pergamon.

Melnikov, D. E., Ryzhkov, I. I., Mialdun, A. & Shevtsova, V. 2008 Thermovibrational convection in microgravity: preparation of a parabolic flight experiment. *Microgravity Sci. Technol.* **20** (1), 29.

Melnikov, D. E. & Shevtsova, V. M. 2005 Liquid particles tracing in three-dimensional buoyancy-driven flows. *Fluid Dyn. Mat. Process.* **1** (2), 189.

Mialdun, A., Ryzhkov, I. I., Melnikov, D. E. & Shevtsova, V. 2008*a* Experimental evidence of thermal vibrational convection in a non-uniformly heated fluid in a reduced gravity environment. *Phys. Rev. Lett.* **101**, 084501.

Mialdun, A., Ryzhkov I. I., Melnikov D. E. & Shevtsova, V. 2008*b* Experimental evidence of thermovibrational convection in reduced gravity. *Space Res. Today* **171**, 4.

Mialdun, A. & Shevtsova, V. 2008 Development of optical digital interferometry technique for measurement of thermodiffusion coefficients. *Intl J. Heat Mass Transfer* **51**, 3164.

Naumann, R. J. 2002 Transport from higher order g-jitter effects. *Ann. NY Acad. Sci.* **974**, 29.

Naumann, R. J., Haulenbeek, G., Kawamura, H. & Matsunaga, K. 2002 The JUSTSAP experiment on STS-95. *Microgravity Sci. Technol.* **13** (2), 22.

Pallares, J., Arroyo, M. P., Grau F. X. & Giralt, F. 2001 Experimental laminar Rayleigh–Bénard convection in a cubical cavity at moderate Rayleigh and Prandtl numbers. *Exp. Fluids* **31**, 208.

Savino, R. & Monti, R. 1998 Improving diffusion-controlled microgravity experiments by facility orientation. *Proc. IMechE* G **212** (6), 415.

Savino, R. & Monti R. 2001 Fluid-dynamics experiment sensitivity to accelerations prevailing on microgravity platforms. In *Physics of Fluids in Microgravity* (ed. R. Monti), chap. 15, pp. 515–559. Taylor & Francis.

Savino, R., Monti, R. & Piccirillo, M. 1998 Thermovibrational convection in a fluid cell. *Comp. Fluids* **27** (8), 923.

Shevtsova, V., Melnikov, D. & Legros, J. C. 2004 The study of stationary and oscillatory weak flows in space experiments. *Microgravity Sci. Technol.* **15** (1), 49.

Shevtsova, V., Melnikov D., Legros, J. C., Yan, Y., Saghir, Z., Lyubimova, T., Sedelnikov, G. & Roux, B. 2007 Influence of vibrations on thermodiffusion in binary mixture: a benchmark of numerical solutions. *Phys. Fluids* **19**, 017111.

Tritton, D. J. 1988 *Physical Fluid Dynamics*. Clarendon.

Zavarykin, M. P., Zorin, S. V. & Putin, G. F. 1988 On thermoconvective instability in vibrational field. *Doklad. USSR Acad. Sci.* **299** (2), 309.

Zenkovskaya, S. M. & Simonenko, I. B. 1966 Effect of high-frequency vibration on convection initiation. *Fluid Dyn.* **1** (5), 51.

Zyuzgin, A. V., Ivanov, A. I., Polezhaev, V. I., Putin, G. F. & Soboleva, E. B. 2001 Convective motions in near-critical fluids under real zero-gravity conditions. *Cosmic Res.* **39** (2), 175.